A biocompatible SiO2/ZnO coating with enhanced antibiofilm properties for dental applications

Applied Surface Science 690 (2025) 162590

Contents lists available at ScienceDirect

Applied Surface Science

journal homepage: www.elsevier.com/locate/apsusc

Full Length Article

A biocompatible SiO_2/ZnO coating with enhanced antibiofilm properties for dental applications

Ehsan Shakerinasab [a,b], Sara Ferraris [c], Sergio Perero [c], Giacomo Maculotti [d], Maurizio Galetto [d], Anna Luganini [e], Martina Perin [e], Federico Mussano [f], Farshad Sohbatzadeh [a,b], Silvia Spriano [c,*]

[a] Department of Atomic and Molecular Physics, Faculty of Science, University of Mazandaran, Babolsar, Iran
[b] Plasma Technology Research Core, Faculty of Science, University of Mazandaran, Babolsar 4741695447, Iran
[c] Department of Applied Science and Technology, Politecnico di Torino, Corso Duca degli Abruzzi 24 10129, Torino, Italy
[d] Department of Management and Production Engineering, Politecnico di Torino, Corso Duca degli Abruzzi 24 10129, Torino, Italy
[e] Department of Life Sciences and Systems Biology, University of Torino, Via Accademia Albertina 13 10123, Torino, Italy
[f] Bone and dental Bioengineering Laboratory, CIR Dental School, Department of Surgical Sciences, University of Turin, Via Nizza 230 10126, Torino, Italy

ARTICLE INFO

Keywords:
Zirconia
Zinc oxide
Coating
Antibacterial
Biocompatibility
Magnetron sputtering
Dentistry

ABSTRACT

Due to its unique properties, yttrium-stabilized tetragonal zirconia (Y-TZP) is well-known as a high-performance material in dental medicine. However, some issues are still open: the interaction of the implant materials with surrounding tissues (osseointegration), the coupling with different biomaterials in the final device assembly (e.g. metal-ceramic dental restorations), and the ability to control bacterial colonization. Herein, we were focused on developing SiO_2/ZnO layers deposited by a co-sputtering technique on Y-TZP substrate and investigating the antifouling effects of the layer. The morphological and chemical characterization of the samples was performed using conventional characterization techniques including FESEM, EDS, XPS, FTIR, water contact angle, and release tests. The hardness of the samples was investigated using the nanoindentation test. The results confirmed the successful deposition of the SiO_2/ZnO layer on the surface of Y-TZP and an increase in the hardness (19 %) of the SiO_2-coated sample by introducing ZnO. The cytocompatibility of the coating was investigated on adipose-derived mesenchymal stem cells (ASCs) evidencing that the developed coating has basic requirements for biological and dentistry applications due to its cytocompatibility. The antibacterial effect of the coating on Y-TZP was investigated against an oral bacterial strain of *Enterococcus faecalis* of clinical interest, used as a model organism with a significant positive outcome (~70 % of bacteria biofilm reduction).

1. Introduction

Nowadays, yttrium-stabilized tetragonal zirconia (Y-TZP) is well known in medicine due to outstanding biocompatibility, high mechanical performance, and aesthetic characteristics (color and opacity) that mimic natural teeth appearances [1,2]. Also, it is the main dental material in dental implant abutments and indirect restorations [3]. The range of applications of Y-TZP in the dental-medicine field is constantly expanding including implant fixtures, implant abutments, and crown restoration [4,5].

However, the success of Y-TZP in permanent implants and prosthesis is dependent on numerous factors including the interaction of the implant materials with the surrounding tissue (osseointegration), and the coupling with different biomaterials in the final device assembly (e.g. metal-ceramic dental restorations). Furthermore, the resistance of the implant and prosthetic surfaces against bacterial colonization is still an unmet clinical request [6]. Clinical studies show bacterial colonization of surfaces and subsequent biofilm formation during and immediately after implant surgery [7]. These bacterial infections and biofilm formation lead to the destruction of adjacent tissue and ultimately possible implant failure [8]. Also, they are the main reasons for dental caries, periodontal, and *peri*-implantitis disease [5,9]. On the other hand, biofilm that forms on a surface provides a protective barrier for bacterial infections. Thus, disinfection treatments are not easy to perform after the biofilm formation [10].

Numerous strategies have been performed by scientists to inhibit the biofilm formation on the implant and prosthetic surfaces [11–14]. These studies include using antioxidants [15], biofilm matrix-degrading agents

* Corresponding author at: Department of Applied Science and Technology, Politecnico di Torino, Corso Duca degli Abruzzi 24 10129 TORINO, Italy.
E-mail address: silvia.spriano@polito.it (S. Spriano).

https://doi.org/10.1016/j.apsusc.2025.162590
Received 10 December 2024; Received in revised form 20 January 2025; Accepted 29 January 2025
Available online 31 January 2025

[16], quorum sensing inhibitors [17], and antibiofilm coatings [18] which inhibit biofilm formation. Among them, the most commonly used strategy entails an antibiofilm coating approach for preventing the first steps of biofilm infections. The strategy focuses on the surface properties of the material itself and comprises preventing bacteria attachment on the surface and killing the bacteria that come into contact with the surface of the material. In this strategy, the chemical composition, surface topography, roughness, wettability, and charging of material surfaces are improved by coating the surface with antibacterial materials [19,20].

Many metals have been tested as antimicrobial coatings, including silver, zinc, copper, gold, and their oxide-based particles. Due to their small size and large surface-to-volume ratio, these materials provide prolonged and strong antimicrobial and antibiofilm properties [21,22]. The main unmet clinical request is to find a balance between cytocompatibility and antibacterial action. Zinc oxide attracted attention for its distinctive properties in dentistry applications including non-toxicity to mammalian cells, great resistance to corrosion, cost-effectiveness, widespread availability, environmental stability, and transparency for visible light. Zn and its compounds are used in different forms for oral application including oral hygiene products such as toothpaste and mouth rinse to inhibit dental plaque, reduce halitosis, and prevent calculus formation [23]. Also, Zn is one of the most effective elements for the inhibition of *Streptococcus mutans* as the main cariogenic bacteria in dental caries. However, the antibacterial properties of zinc oxide are higher than those of Zn, and it is more commonly used compared to Zn. [24–26]. Overall, the three main mechanisms of antimicrobial activity of ZnO are the release of Zn^{2+} ions, formation of free radicals and ROS, and direct attachment between ZnO and bacteria by electrostatic interactions which damage the cell membrane [25]. These mechanisms are of great relevance because they are less prone to the development of bacterial resistance than specific biological pathways.

From the chemical and physical standpoints, the presence of Zn and ZnO in a coating leads to increased toughness, mechanical reinforcement, and chemical stability. Nevertheless, a too high content of Zn may have some inverse effect decreasing the mechanical properties of the coating [27]. More importantly, when trying to achieve maximum antimicrobial performance through an increase in Zn and ZnO content, the cytocompatibility of the layer may be lost. So, the balance of the layer composition is always a key factor to have both antimicrobial and cytocompatibility properties [28].

One of the potential materials that can be used alongside Zn in a dental coating is silicon dioxide. SiO_2 coating on dental materials, including Y-TZP, is widely used due to its potential to improve the surface hardness of the substrate, increase the adhesion of Y-TZP to other implant and prosthetic materials, and reduce susceptibility to bacterial adhesion [29–31].

The deposition of a nanometric silica layer onto zirconia for dental crowns to improve the bonding strength with resin has been explored by means of sol–gel deposition [32] and atomic layer deposition [30] coupled with silanization. An alternative solution, reported for improving bonding strength, is represented by alumina-based nanocoatings obtained by a chemical route [33]. In any case, no antibacterial activity is expected for these strategies. The use of non-thermal atmospheric pressure plasma (NTAPP) treatment has been proposed to combine an enhancement in the bonding strength of zirconia to resin together with the reduction of bacterial contamination [33], however, this technique has a limited duration (max. 48 h).

Herein, we were focused on developing SiO_2/ZnO layers deposited by a co-sputtering technique on Y-TZP substrate and investigating the mechanical properties, cytocompatibility, and antifouling effects of the layer. The approach is novel because the explored silica coatings on zirconia for prosthetics or implants lack in stability and have no antibacterial properties. Still, the combination of zinc oxide, widely investigated as an antibacterial material in many biomedical applications [34], with silica has never been explored in a coating on zirconia. Moreover, the sputtering technique has not yet been used for the obtainment of these composite-coating on dental zirconia for this purpose.

The combination of silica and zinc oxide has been reported for antimicrobial coatings on textiles [27], but not on dental zirconia, to the best of the authors' knowledge. The presence of the silica matrix is expected to protect zinc oxide from an excessive release and stabilize it on the zirconia surface. In addition, co-sputtering represents a green approach for coating deposition which avoids the employment of toxic chemicals and the production of chemical waste. More precisely, a co-sputtering technique was used to depose a SiO_2/ZnO layer with different Zn contents (11 and 44 wt%) on a commercial Y-TZP substrate. The biofilm formation on developed SiO_2/ZnO layers was compared to pristine Y-TZP substrate using clinical oral bacterial strains. In the final step, the cytocompatibility and mechanical strength of our developed SiO_2/ZnO layers were investigated.

2. Materials and Methods

2.1. Surface coating on Y-TZP

In this work, a co-sputtering process was employed as a source for the surface coating of Y-TZP. A preliminary work was performed to optimize co-sputtering conditions and experimental parameters for the coating: it is described in the Supplementary section. The parameters used for the optimized samples are listed in Table 1. F1 is the control sample (zirconia substrate without coating), the F2 sample is a pure SiO_2 coating without zinc, and the F3 and F4 samples are SiO_2 coatings enriched with different amounts of zinc, a low amount for F3 and a high amount for F4. Samples were polished sequentially using a polishing machine with silicon carbide papers of increasingly finer grit sizes, commencing with 400 grit and progressively refining the surface finish through the use of 800, 1200, and 4000 grit. Silicon dioxide (Sigma-Aldrich, 99.99 % purity) and zinc (Sigma-Aldrich, 99.99 % purity) targets were used for depositions. Depositions were performed with a Kenosistec™ custom design sputtering equipment with three independent cathodes powered by separate generators of different types (DC and RF) and with different powers. A radio frequency (RF) power supply with a constant power of 250 W power was applied to the magnetron cathode with the SiO_2 target, while direct current (DC) powers with different powers (5 W, and 40 W) were applied to the magnetron cathode of the zinc target. The working pressure was 10^{-2} mbar to reduce the Zn evaporation. Argon (Ar) and Oxygen (O_2) gases with a purity of 99.9 % were used as the feed gases for the ignition of the plasma with a flow rate of 50 sccm, and 10 sccm, respectively. Also, all the depositions were performed for 90 min under a pressure of 5.5 dPa. Before the coating by co-sputtering, the substrates were ultrasonically cleaned with ethanol 99 % for 5 min, in deionized water for 10 min, and dried under atmospheric pressure.

Table 1
Co-sputtering conditions and experimental parameters for the coating of different samples (F1, F2, F3, and F4).

		F1	F2	F3	F4
Sputtering gas flow rate	Argon (sccm)	–	10	10	10
	Oxygen (sccm)	–	50	50	50
Power supplied to SiO_2 Sputtering Target		–	RF	RF	RF
Sputtering power of the SiO_2 (W)		–	250	250	250
Power supplied to Zn Sputtering Target		–	–	DC	DC
Sputtering power of the Zn (W)		–	–	5	40
Base Pressure (mbar) of the deposition		–	1.2×10^{-2}	1.2×10^{-2}	1.2×10^{-2}
Deposition time (min)		–	90	90	90

2.2. | physical and chemical characterizations

The morphological analysis of the samples was performed by Field-Emission Scanning Electron Microscope (FE-SEM, QUANTA INSPECT 200, Zeiss SUPRA 40), at different magnifications at 3 kV. Compositional analysis (both area analysis and maps acquisition) was performed by energy dispersive spectroscopy (EDS, EDAX PV 9900TM) at 15 kV and the magnification of 100 x.

The surface roughness of the samples was measured using a coherence scanning interferometer (NewView9000, Zygo, Middlefield (CT), USA) with a 20 × magnification Mirau objective. According to ISO 25178–2, raw data were corrected for planarity, by implementing as F-operator a least square first order fitting corrected by subtraction, and LS-surface surface topography height parameters evaluated – as per ISO 25178–2 – considering the application of S-filter and L-filter, both implemented as Gaussian filters of order 1 robust to end-effect, with a nesting index of 1.5 μm and 0.150 mm, respectively, as per ISO 25178–3. Ten random locations per sample were measured and analyzed.

The chemical characterization was conducted by X-ray photoelectron spectroscopy (XPS, PHI 5000 VERSAPROBE, PHYSICAL ELECTRONICS). Both survey spectra and high resolution of C, Si, O, and Zn regions were acquired. All the high-resolution spectra were referenced by setting the hydrocarbon C1s peak to 284.80 eV for charging effect compensation.

Fourier Transform InfraRed (FTIR-ATR) spectra were acquired in the range of 500–4000 cm^{-1} with a resolution of 4 cm − 1 using an attenuated total reflectance (ATR) spectrometer (Thermo Scientific Nicolet iS50, Thermo Fisher Scientific, Milano, Italy) equipped with a diamond crystal ATR accessory.

Static mode contact angle measurements were used to assess the wettability of the uncoated and coated Y-TZP substrates with a Kruss G10 instrument device. The contact angle measurement was performed by depositing a 5 μl ultra-pure water droplet (ARIUM PRO UV SARTORIUS; specific resistivity 18.2 MΩcm; TOC < 2 ppb; $\gamma = 72$ mN/m) onto the surface of the samples, under atmospheric conditions at room temperature, and capturing an image after 5 s.

2.3. Mechanical surface properties

The mechanical surface properties of the samples were evaluated using an Anton Paar NHT3 nanoindenter, compliant with the ISO 14577–4 standard. The platform frame compliance and indenter geometry were calibrated using NPL SiO2 and W reference material showing a relative measurement uncertainty of 6 % for the indentation hardness and 2 % for the indentation modulus. The continuous multi-cycle (CMC) loading mode was employed for the nanoindentation test, with 16 indentations performed on each sample and 15 cycles comprising 10 s of load, 15 s of hold, and 10 s of unloading, which is necessary to compensate for creep. The quadratic load step was maintained within the range of 0.5 to 10 mN to ensure consistent and accurate measurement of the samples' surface mechanical properties. The CMC mode allows a profile of the mechanical properties as a function of depth. Each unloading curve is fitted with a power law, as per ISO 14577–1, fitting from 98 % to 80 % of the maximum force reached during the cycle to estimate the contact stiffness. The trend of the in-depth mechanical characterization is then analyzed as per ISO 14577–4 to deconvolute the effect of the substrate and achieve the characterization of the coating.

2.4. Leaching test in water.

The amount of zinc ions released by the coatings on Y-TZP was evaluated by means of leaching tests in ultra-pure water droplet (ARIUM PRO UV SARTORIUS; specific resistivity 18.2 MΩcm; TOC < 2 ppb). Samples of an average size of $0.5 \times 1 cm^2$ were immersed in 30 mL of ultrapure water at 37 °C, with the coated surface face up. The solutions were analyzed from the time until 7 days using a photometer for zinc ions (Hanna Instruments, Woonsocket, RI, USA). The concentration of zinc ions was determined in ppm. Each measurement was repeated two times to ensure accuracy, and the average amount was reported.

2.5. Cell viability assays

ASCs (adipose-derived mesenchymal stem cells) are an established cell model for in vitro characterizing the biological response elicited by dental materials, as they represent the precursors of osteoblast and osteocytes, i.e. bone-forming cells, the major tissue interface of the dental fixtures. ASC52telo (ATCC, Manassas, VA, USA) were used to evaluate the toxicity of the coated layers. Cells were kept in a Mesenchymal Stem Cell Basal Medium supplemented with Mesenchymal Stem Cell Growth Kit (ATCC). Sample F1 was used as the control sample. 25,000 ASCs were plated on discs and maintained in culture. The cell viability was evaluated after 24 h, 48 h, and 72 h by CellTiter-Glo® (Promega, Madison, WI, USA) which allows for a dose of the luminescence (by luminometer) associated with the ATP release in the cell medium, which is related to viability of the cells. For fluorescent imaging, cells were seeded on different surfaces and fixed with a 4 % paraformaldehyde solution after 24 h. Cells were then permeabilized with TBS 0.1 % Triton X-100 (Sigma-Aldrich, St. Louis, MA, USA) and stained with Alexa 488-Phalloidin (Life Technologies, Carlsbad, CA, USA) to detect the cytoskeleton and DAPI (Sigma-Aldrich, St. Louis, MA, USA) for the nuclei. Images were acquired with a Nikon Eclipse Ti-E microscope using a Nikon Plan 40×/0.10 objective (Nikon Instruments, Amsterdam, the Netherlands).

2.6. | bacterial biofilm evaluation

Quantification of bacterial biofilm was performed by a direct method as described in Genova et al., 2022 [34]. A single colony of standard E. faecalis (ATCC 29212) was grown overnight in 10 mL of Luria Bertani (LB) broth (Sigma Aldrich, St. Louis, MO, USA) at 37 °C in agitation 220 rpm. The day after, bacteria were subcultured until an optical density (OD600) of 0.6 was reached, corresponding to 2 × 108 colony-forming units (CFU)/mL, approximately. Each sample was incubated with 1 ml of bacterial suspension in a 24-well plate by using a shaking rotator (80 rpm) at 37 °C for 24 h. To remove non-adherent bacteria, samples were rinsed in a sterile phosphate-buffered saline solution (PBS, pH 7; Sigma Aldrich, St. Louis, MO, USA) four times and then placed in a sterile eppendorf containing 1 ml saline and vortexed for 10 s, at 25 Hz two times. Each sample was, then, transferred to a sterile tube containing 1 ml saline solution and sonicated at 80 kHz with a power output of 250 W x 5 min. Then, samples were vortexed for 5 s again, and afterwards, a volume of 0.4 ml of 10-fold dilutions of each suspension was plated by spread-plating onto an LB agar plate for colony counting at 37 °C for 24 h. Following incubation, the colony-forming units per milliliter (CFU/mL) were calculated using the formula: CFU/mL = [Number of colonies × Dilution factor]/Volume plated (mL). One well per plate was inoculated with bacterial suspension, that was vortexed and sonicated as described above, as a control for bacteria vitality after the procedure used.

2.7. Statistical analysis

One-way analysis of variance (ANOVA) and Bonferroni test were utilized to compare the mean of variables in different sections of the paper using SPSS Statistics software (v.25 IBM, USA). For that, the significance level for all trials was set to $\alpha < 0.05$.

3. Results and discussion

3.1. Compositional and morphological characterization

A preliminary work for optimizing the process parameters was performed and it is described in the Supplementary section. At the end of this work, samples F3 and F4 were selected as the most interesting in terms of different coating compositions and they were fully characterized: results are here reported. The surface morphology of the pristine substrate and selected SiO_2/ZnO coated samples is shown in Fig. 1. The pristine Y-TZP (sample F1) had a relatively smooth surface with some small striations due to the polishing of the substrate.

After the deposition of SiO_2/ZnO coating, a dense granular morphology was formed on the surfaces of all deposited samples (samples F2, F3, and F4) with a similar appearance that is the typical structure for sputter deposited coatings [35]. For all coated samples, the FE-SEM images showed a uniform coverage of the layers on the surface.

By comparing the images, higher agglomeration on the surface was observed for sample F4. This may be related to the presence of ZnO submicrometric particles embedded within the SiO_2 matrix.

The results of surface topography are detailed in Table 2 and confirm the FESEM findings. In surface topographical images (Fig. 1), there is no significant difference between the roughness of control and coated surfaces. The coating using the co-sputtering technique did not

Table 2
Average roughness, kurtosis, and skewness of the surfaces. Measurements were performed on a 400 μm × 400 μm area.

Samples	Average roughness Sa (μm)	Standard deviation of Sa (μm)	Kurtosis Ssk	Skewness Sku
F1	0.103	0.041	5.8	−1.1
F2	0.121	0.049	5.8	−0.9
F3	0.141	0.099	2.9	1.9
F4	0.136	0.058	5.8	−1.4

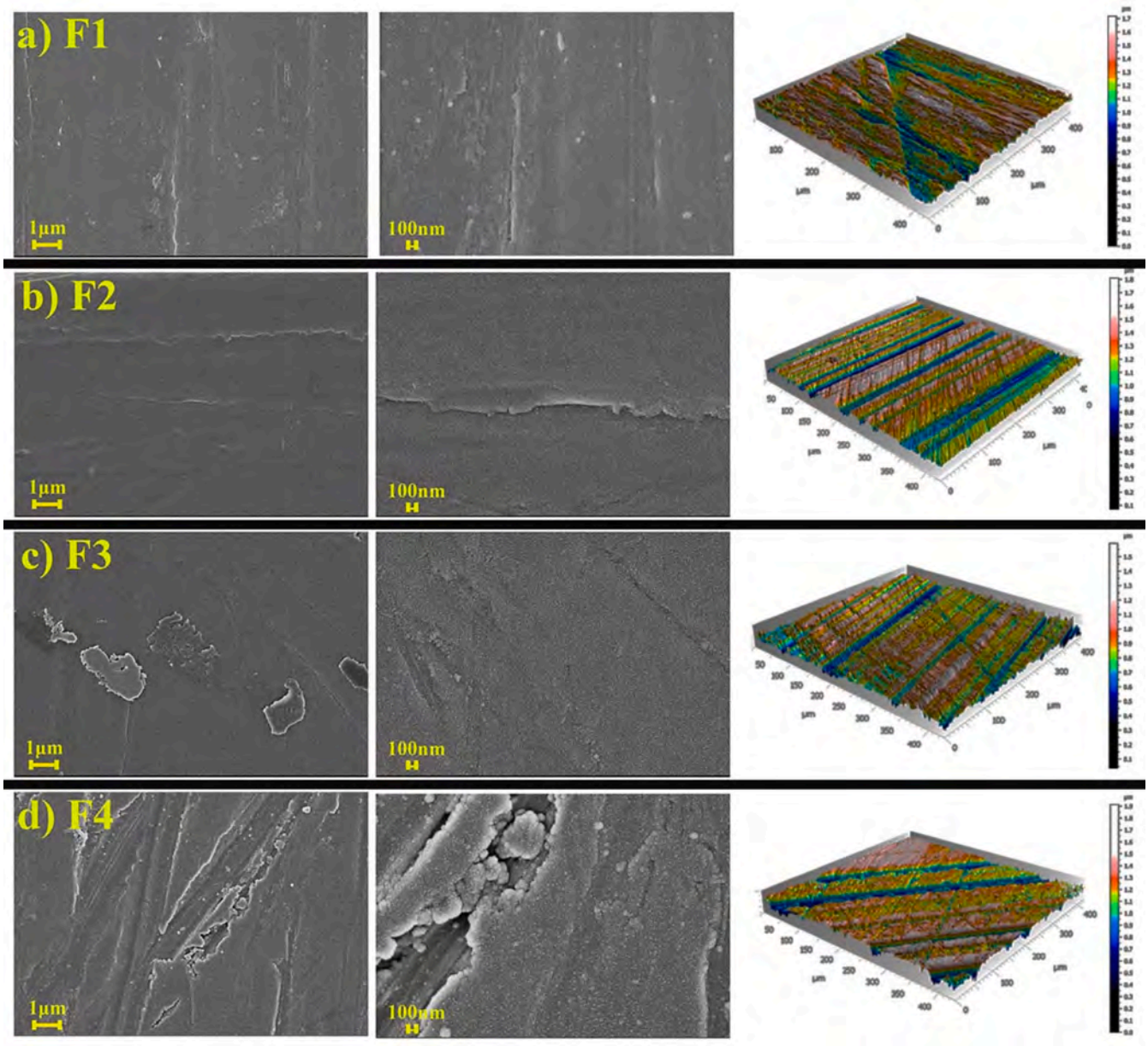

Fig. 1. FE-SEM images of a) F1 b) F2, c) F3, and d) F4 samples at different magnifications (markers of 1 μm and 100 nm) along with surface topographical images (400 μm × 400 μm area).

significantly affect roughness but accurately reproduced the substrate topography, as previously observed by the authors [36], and confirmed by one-way ANOVA on the treatment (p-value > 0.05). The measured average roughness, assessed in terms of Sa, agreed with polishing with grit 4000 silicon carbide papers. An average roughness lower than 0.2 μm is requested to investigate biofilm formation on surfaces comparing different chemical compositions and avoiding any increase in bacterial colonization due to morphological issues. The prepared samples respond to this requirement. Standard deviations are low, compared to the average roughness, evidencing uniformity of surfaces; a polishing defect was present on F3 affecting a bit the results. Kurtosis values around 5 evidence that the distribution of the heights of points on the surfaces had heavier tails than a normal Gaussian distribution (expected Kurtosis value equal to 3) but this is usual for hand-polishing. A negative value of skewness was expected for sample F1 (control) because hand-polishing is based on material removal and introduces valleys on the surface rather than asperities. On the contrary, positive values of skewness on coated samples agreed with a coating method based on the deposition of

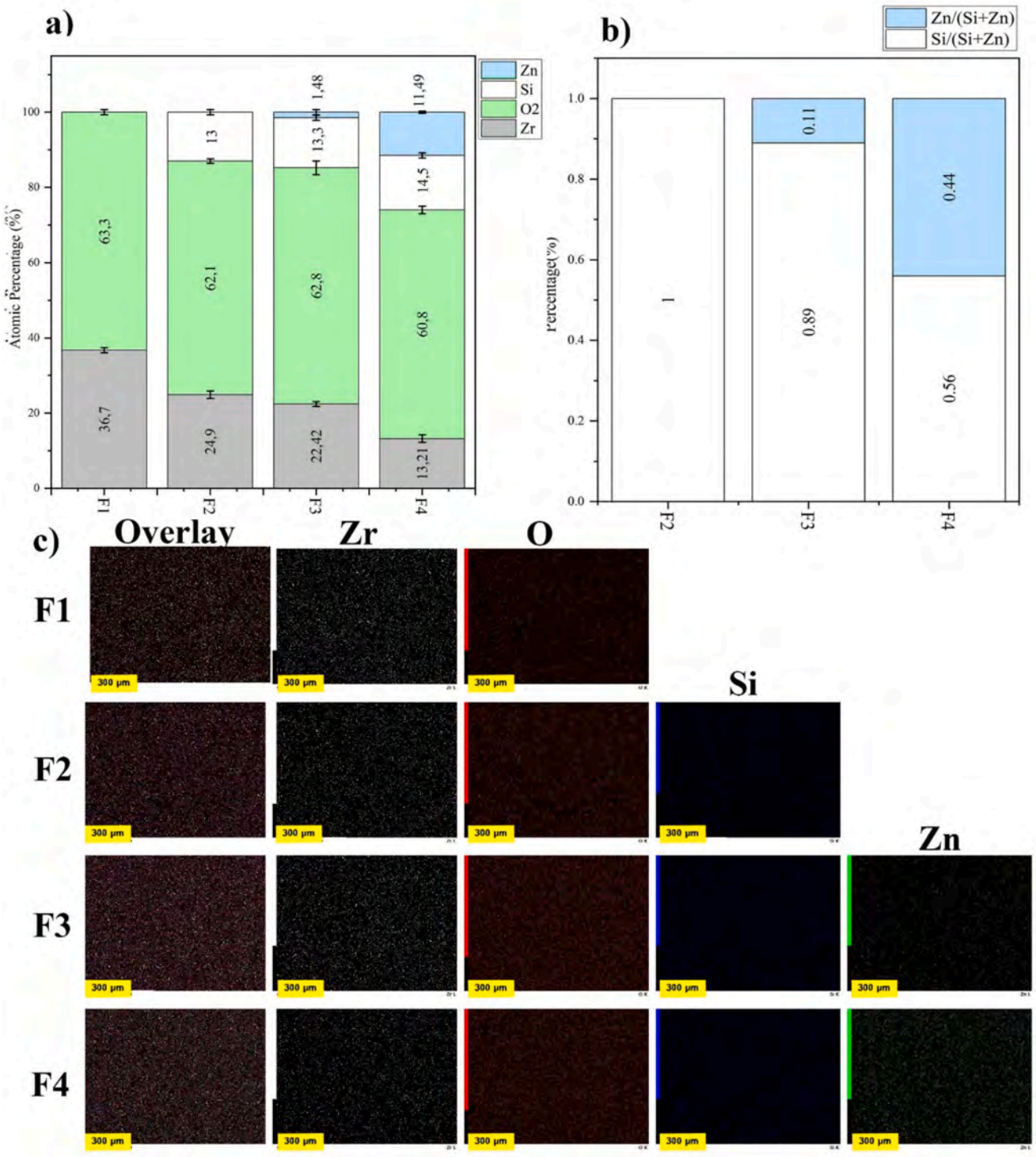

Fig. 2. EDS data analyses of all samples i.e., (a) atomic percentage for O, Zr, Si, and Zn elements (b) calculated Zn/(Zn + Si) and Si/(Zn + Si) ratios based on the EDS data, and c) elemental map analysis of all samples.

material on the surface as magnetron sputtering is (Table 2).

Fig. 2 depicts the results of EDS data analysis for pristine and sputter-coated Y-TZP samples. The atomic percentage ratio of Zr, O, Si, and Zn elements was calculated based on the EDS spectra and reported in Fig. 2a. Only Zr and O were detected on the pristine Y-TZP sample, which were related to Y-TZP, whereas Si and Zn peaks appeared in the spectra after the deposition of SiO_2 / ZnO coatings. The amount of Zr has a decreasing trend comparing F2 and F4, evidencing an increase in the coating thickness on this sample. The Zn/(Zn + Si) and Si/(Zn + Si) atomic ratios were calculated from the EDS data and reported in Fig. 2b for the three deposited samples (F2, F3, and F4). The composition of the F2 sample, analyzed by EDS, confirmed the deposition of bare silica on the surface of Y-TZP, whereas the samples F3 and F4 revealed 89 % Si/(Zn + Si) and 11 % Zn/(Zn + Si) or 56 % Si/(Zn + Si) and 44 % Zn/(Zn + Si), respectively.

Fig. 2c depicts the spatial distribution of coated elements through elemental map analysis. Based on the results, the F2 sample was composed of pure silica, and the F3 and F4 samples also contained Zn and Si. The elements were uniformly distributed on all samples and coatings completely covered surfaces. The atomic ratio and elemental maps for all samples were related to average values obtained from three different EDS scan repeats at low magnification (at 100 ×).

FTIR studies were carried out to acquire an insight into the surface composition of the deposited layers on the Y-TZP substrate. The infrared spectra of F1 to F4 samples in the range of 400 cm^{-1} to 4000 cm^{-1} are shown in Fig. 3a. All samples showed almost similar spectra. However, some alterations in the peak intensity and positions can be seen in the overlay view of the spectra within the ranges of 400 cm^{-1}–1500 cm^{-1} in Fig. 3b. In all samples, an intense unresolved band between 520 cm^{-1} and 800 cm^{-1}, with the center at 632.8 cm^{-1}, exists, which was attributed to the Zr-O stretching modes of the substrate [37,38]. After the sputter deposition, a wide peak between 1000 and 1250 cm^{-1} intensely grew. The peaks at ~1076 cm^{-1}, along with an associated peak at ~1217 cm^{-1}, were assigned to the in-phase and out-of-phase stretching modes of Si-O groups [39,40]. The results suggested the formation of the SiO_2 coating layer on the surface of the F2 to F4 samples. Also, some shoulders started to grow in the range of 500 cm^{-1} to 750 cm^{-1} for the sample F4. These peaks were located at ~554 cm^{-1}, ~575 cm^{-1}, and ~592 cm^{-1}, which arises from the stretching mode of Zn − O [41–43] which confirms the presence of zinc oxide in the F4 sample. These shoulders did not appear in the F3 sample because of the low content of zinc elements in this sample and the thinner coating (as was confirmed by EDS results in Fig. 2a and 2b). As depicted from the FTIR results, a SiO_2/ZnO coating was successfully deposited on the surface of the samples with better evidence of ZnO on the F4 sample.

XPS analyses were performed for additional insight into the deposited layer on the Y-TZP substrate. The full survey XPS data of the F1 to F4 samples are depicted in Table 3. The F1 sample (control) showed the signals of Zr3d5, Zr3p1, Zr3p3, O1s, and OKLL peaks at ~181 eV, ~345 eV, ~331 eV, ~525 eV, and ~977 eV respectively, which correspond for Zr and O elements in the control Y-TZP substrate, as expected. For the F2 sample, two main peaks at about ~101 eV, and ~153 eV were added to the spectrum which can be assigned to Si2p and Si2P. The presence of Si indicated the successfully deposited pure silica layer on the surface of

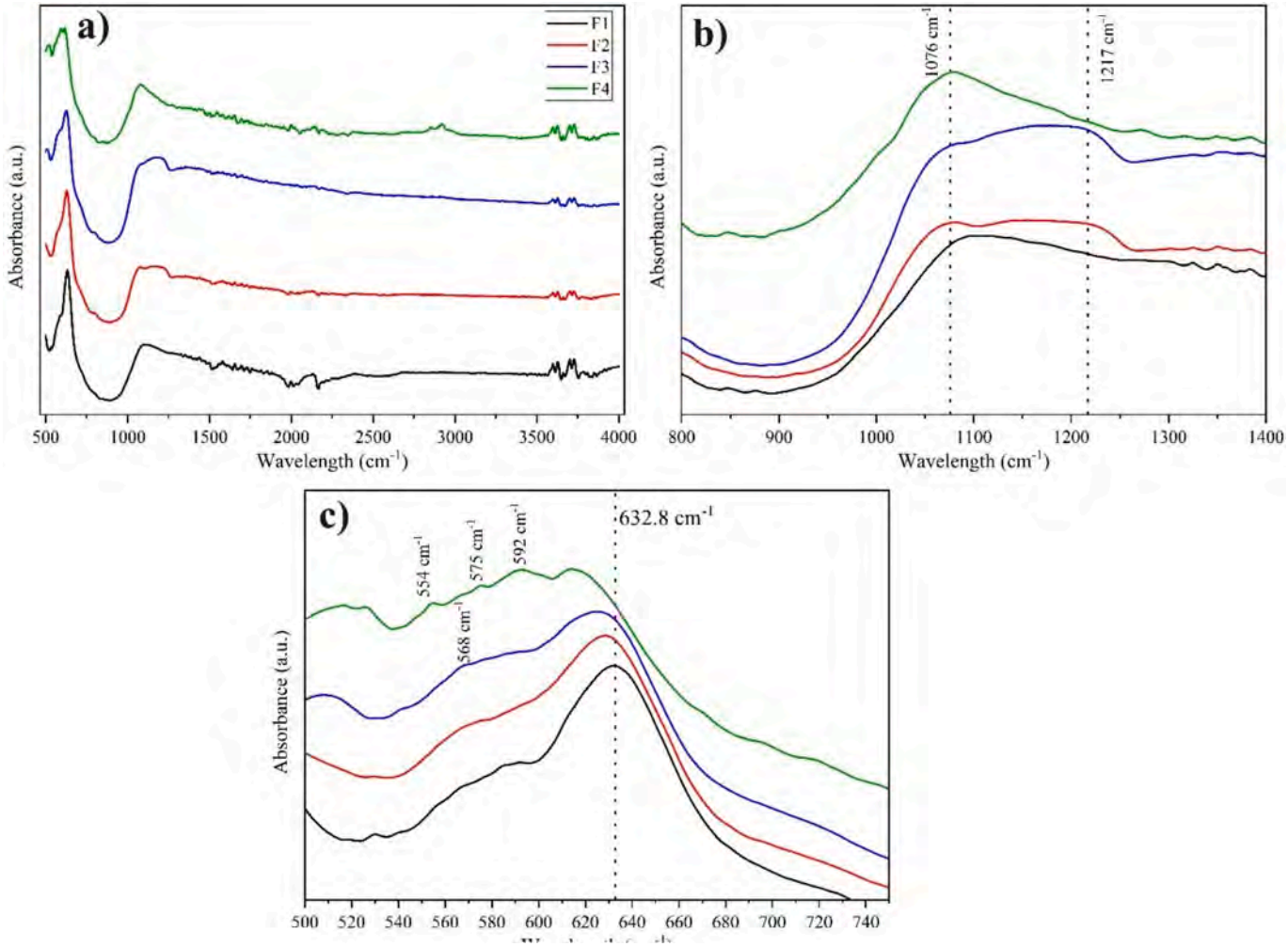

Fig. 3. Full-range ATR spectra of the F1-F4 samples, overlay view of the F1-F4 samples within the ranges of a) 500–4000 cm^{-1}; b) 800–1400 cm^{-1}, c) 500–750 cm^{-1}.

Table 3
Elemental Composition (%) from Survey XPS Spectrum for Samples F1, F2, F3, and F4 samples.

	Binging energy (eV)	F1 (%)	F2 (%)	F3 (%)	F4 (%)
O1s	~529	25.20	51.77	34.98	23.81
OkLL	~977	15.01	12.32	10.51	2.73
C1s	~283	9.56	15.04	15.52	
Zr3d5	~181	26.15	–	–	–
Zr3p3	~331	14.24	–	–	–
Zr3p1	~345	9.84	–	–	–
Si2p	~101	–	9.85	5.97	0.35
Si2s	~153	–	11.02	9.50	4.24
Zn LMM	~474	–	–	0.30	3.88
Zn LMM	~497	–	–	4.15	15.20
Zn2p3	~1022	–	–	10.11	14.15
Zn2P1	~1044	–	–	8.98	4.99

the Y-TZP sample, which is in good accordance with the EDS and elemental map results. In F3 and F4 samples, in addition to appearing Si2p and Si2P at ~101 eV, and ~153 eV, four main peaks appeared at ~474 eV, ~497 eV, ~1022 eV, and ~1044 eV which were assigned to ZnLMM, ZnLMM, Zn3p1, and Zn3p3 respectively. These spectra indicated that the SiO_2/ZnO layers were successfully deposited. The two symmetric peaks at ~1021.0 eV and ~1044 eV, which correspond to the Zn2p3 and Zn2p1, are attributed in the literature to Zn^{2+} ions in SiO_2/ZnO hybrid nano chains [44,45]. Zr peaks disappeared from the deposited layer (F2 to F4 samples) in XPS survey spectra which can be related to the presence of a coating thicker than the penetration depth of XPS analysis. Moreover, the C1s peak can be detected in the survey spectrum of all samples, which can be assigned to the residual amount of organic additives or adventitious contaminations.

To further understand the chemical states of different elements within the deposited layer, detailed XPS analysis was carried out on Zr, Si2P, O1s, and Zn2p3 high-resolution peaks. Fig. 4a and 4b show deconvolutions of the Zr 3d5 and O1s regions of the sample F1, respectively. The Zr 3d peak of sample F1 can be fitted mainly by two sub-peaks at ~182.1 eV, and ~184.4 eV arising from 3d5/2 and 3d3/2 spin–orbit splitting, respectively: these binding energies correspond to ZrO_2. Also, the O1s spectrum of sample F1, centered at ~529 eV binding energy, can be fitted with two curves composed of the Zr-O bond at ~529.7 eV and O–H bond at ~531.3 eV. The peak at 531.3 eV can be assigned to either absorbed OH due to surface contaminants of the sample or lattice oxygen. The XPS results of sample F1 were completely consistent with the XPS spectra of conventional Y-TZP [28,46,47]. For the F2 sample (Fig. 4c), the fitting evidenced two sub-peaks centered at ~103.5 eV, and ~104.5 eV, which assign to the Si-O (SiO_2) and Si-OH bond, respectively. Also, for the O1s spectrum of the sample F2 (Fig. 4d), the coated layer can be fitted mainly by two sub-peaks located at ~532.7 eV and ~534.1 eV, which are assigned to the Si-O (SiO_2) and Si-OH bonds, respectively.

These two sub-peaks are matched with the sub-peaks that appeared in the Si2P fitted curve. These results indicate the formation of SiOx film on the surface of Y-TZP [48–50]. The Si2p peak of sample F3 has been deconvoluted into three components (Fig. 4e) at ~104.5 eV, ~103.4 eV, and ~102.9 eV. The peaks located at ~104.5 eV, and ~103.4 eV can be assigned to the Si-OH and Si-O (SiO_2) bonds (as indicated in F2 for the pure silica layer), while the peak at ~102.7 eV is most likely associated with the formation of Si – O – Zn bonds [43]. Also, for the O1s spectra of the sample F3 (Fig. 4f), the peak can be fitted mainly by four sub-peaks located at ~533.8 eV, ~532.5 eV, ~531.7 eV, and ~530.7 eV. The peaks located at ~533.8 and ~532.5 eV can be assigned to the Si-OH and Si-O (SiO_2) bonds (as indicated in F2 for the pure silica layer), and the peak located at ~530.7 eV can be assigned to the lattice oxygen of ZnO (O^{2-}) [51]. The peak located at ~531.7 eV can be assigned to the Si – O – Zn bonds as corroborated by an additional component revealed in the Si 2p peak fitting curve [43,52,53]. A trend similar to the sample F3 was detected for sample F4. The Si2P peak was deconvoluted into three components (Fig. 4g) at ~103.5 eV, ~102.7 eV, and ~101.9 eV. The peak located at ~103.5 eV can be assigned to the Si-O (SiO_2) bonds (as indicated in the F2 sample for the pure silica layer), while the peaks at ~102.7 eV and ~101.9 eV are most likely associated with the formation of Si – O – Zn bonds. Moreover, in the O1s spectra of the sample F4 (Fig. 4h), the peak can be fitted mainly by four sub-peaks located at ~534.5 eV, ~532.3 eV, ~531.6 eV, and ~530.7 eV. The peaks located at ~534.5 eV, and ~532.3 eV can be assigned to the Si-OH and Si-O (SiO_2) bonds, and the peak located at 530.7 eV can be assigned to the lattice oxygen of ZnO (O^{2-}). Also, the peak located at 531.6 eV is most likely associated with the formation of Si – O – Zn bonds [43,52,53]. The high-resolution Zn3p3 spectra for samples F3 and F4 displayed peaks at binding energies of ~1022.1 eV and ~1022.6 eV, and ~1022.4 eV and ~1023.6 eV, respectively. The binding energy of ~1022.1 eV observed in the F3 sample corresponds to the characteristic value of Zn^{2+} ions (1022.1 eV [54]). However, a small shift in the binding energy was noticed for the F4 sample. This shift can be attributed to the interaction between ZnO and SiO_2 in the composite coating, as confirmed by the additional components in the O1s and Si2p peak fitting curves for both samples. This interaction between ZnO and SiO2 in the composite coating is likely responsible for the enhanced properties observed, such as increased hardness and antibacterial effects[55].

The water contact angle measurement results are reported in Fig. 5. F2 and F3 samples showed increased water wettability compared to pristine Y-TZP samples, while F4 showed the lowest water wettability becoming hydrophobic. The increase in water wettability of F2 and F3 samples can be ascribed to silica-based coatings. More precisely, the responsible functional groups were surface hydroxyl in silica-based coatings and the high affinity of these groups for water [36,56]. However, the increase in the contact angle of F4 can be attributed to the high zinc content of this sample as confirmed by EDS results [57]. Cytocompatibility is strongly associated with wettability and contact angles around or below 60° are requested for cell adhesion [58]. The decrease of contact angle measured on F2 and F3 vs F1 can be considered an interesting advantage for biomedical applications, while hydrophobicity of F4 is a potential issue.

Although the precise mechanism for the antibacterial activity of ZnO is not clear, the release of zinc ions is one of the fundamental mechanisms of its antibacterial performance. Accordingly, the zinc ions released from the SiO_2/ZnO coatings were investigated in ultrapure water. The results are shown in Fig. 5. After 24 h, the amount of ions detected in the water for F3 and F4 was about 0.34 and 0.99 mg/L, respectively. Indeed, the released amount of zinc ions in deionized water was a function of the zinc content on the sample surface. However, the amount of ions detected in the water remained quite constant until the 7 day. It indicates that the zinc ions release happened in less than 24 h in the samples [27]. The Minimum Inhibitory Concentration (MIC) reported for zinc ions is around 768 μg/ml [59,60]. while the Lethal Dose 50 (LD50) around 0.23 mg/l [61]. The comparison between these values and the results of biological tests will be discussed in the following.

Fig. 5 depicts the results of EDS data analysis for F3 and F4 samples after 1, 2, 3, and 7 days of the release test. The atomic percentage of zinc content remained quite constant in F3, after the release at different times, indicating the low ion release from the sample. However, the zinc content significantly decreased for F4 after the one-day release test. It shows that a large release of zinc ions happened quickly for the higher content of zinc (F4) in our developed SiO_2/ZnO layers.

3.2. Surface mechanical properties

Following the coating process, nanoindentation testing was conducted to evaluate the surface mechanical properties of the samples. Results report the mean and expanded uncertainty at a 95 % confidence level. The F2 sample, composed of a pure SiO_2 layer, exhibited an indentation hardness of (8.87 ± 1.10) GPa and an indentation modulus, estimating the Young's modulus, of (98.4 ± 11.7) GPa, aligning with

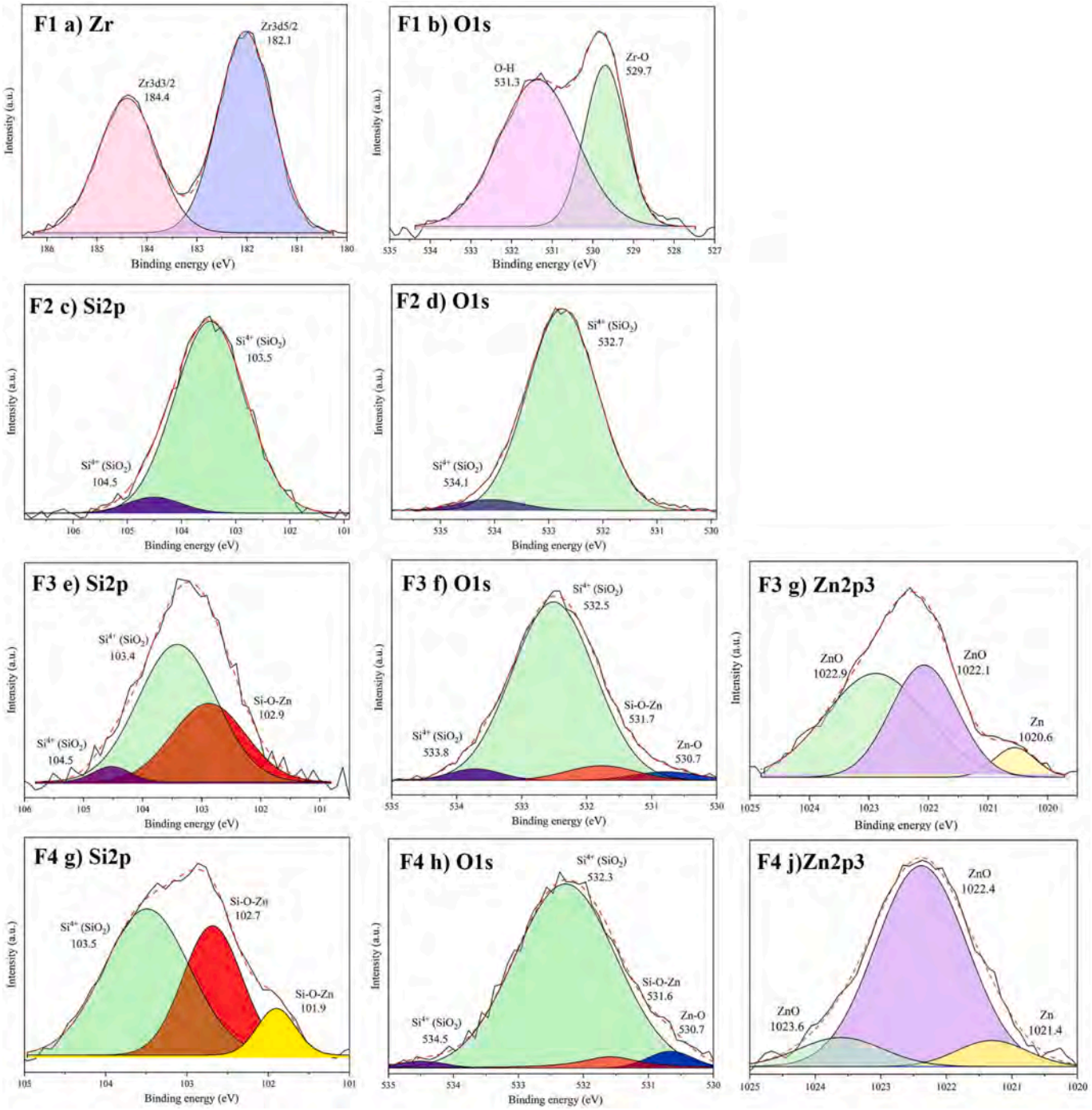

Fig. 4. Curve fitting for XPS spectra of (a) Zr in sample F1, (b) O1s in sample F1, (c) Si2p in sample F2, (d) O1s in sample F2, (e) Si2p in sample F3, (f) O1s in sample F3, (g) Si2p in sample F4, (h) O1s in sample F4, (i) Zn3p3 in sample F3, and (j) Zn3p3 in sample F4.

previously reported values for pure SiO_2 layers [57]. Post-treatment, indentation hardness and indentation modulus values for F3 and F4 samples were found to be (10.52 ± 1.32) GPa, (160.8 ± 14.8) GPa, and (8.3 ± 1.35) GPa, (153.9 ± 18.3) GPa, respectively. Interestingly, the observed data did not reveal a linear correspondence between ZnO content and sample hardness as the ZnO content increased from F3 to F4. While there was no direct relationship established between ZnO content and hardness, the incorporation of ZnO into the SiO_2 layer did result in an overall increase in hardness compared to the pure SiO_2 layer (F2 sample). The observed increase in hardness of the SiO_2/ZnO composite layers compared to the pure SiO_2 layer can be partly attributed to the higher hardness value of ZnO in comparison to SiO_2.

3.3. Cell adhesion and viability

Cell adhesion assays were carried out to analyse how the presence of zinc on deposited samples affects the cell–material interactions: F3 and F4 were selected to evaluate the impact of varying concentrations of ZnO within the SiO_2 matrix. Pristine Y-TZP (F1) was used as a control, being the substrate without the coating and providing a baseline to assess the effects of coatings. F2 was not considered of interest for the biological characterization because silica was not expected to have antibacterial properties considering the literature[62]. The results are depicted in Fig. 6. Cell viability tests conducted on the F3 samples confirmed that this sample is cytocompatible. No cytotoxicity effects were found for this

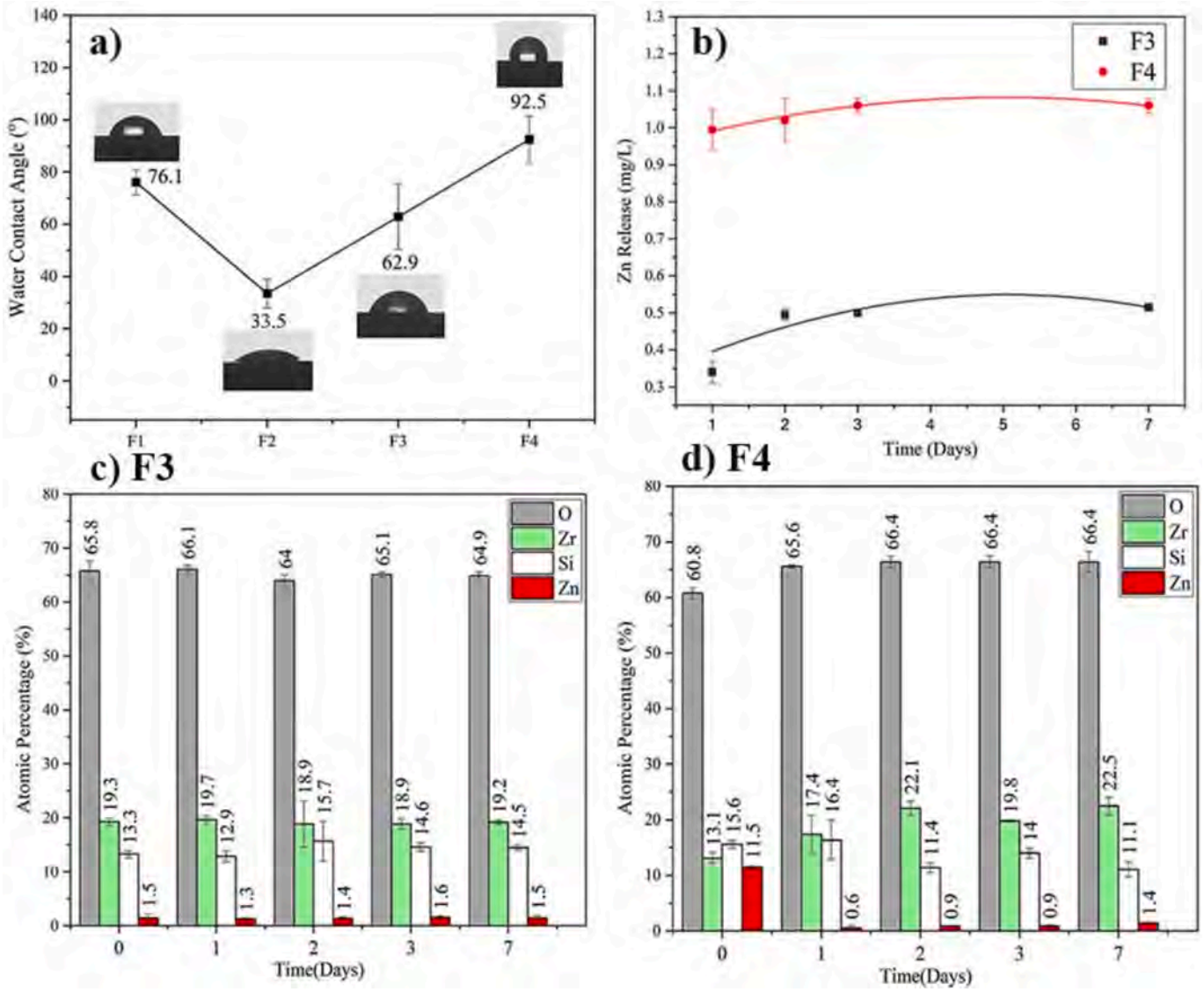

Fig. 5. a) Water contact angles of the samples; b) measurement of the release of zinc ions into water at room temperature from SiO_2/ZnO coatings; c) EDS data analysis on F3 and (d) F4 samples after the 1, 2, 3, and 7 days of the release test.

coated sample and cells sustained cell growth and proliferation within 24 h, 48 h, and 72 h. There was not any statistically significant difference between the pristine Y-TZP (F1) and F3 sample.

However, sample F4 reduced cell proliferation in a statistically significant way after 24 h, 48 h, and 72 h of cell culture. The significant decrease in cell viability for F4 samples was due to the higher percentage of ZnO in agreement with the literature [63,64]. Totally, it could be said that the F3 sample had basic requirements for biological compatibility and implant or prosthetic applications while F4 had not.

These data are in accordance with the values for LD50 (0.23 mg/l Zn^{2+}) reported in the literature [59,61] and the ion release data obtained in this work. In fact, the ion release at 24 h for F3 was close to LD50 while the one for F4 was significantly higher.

The immunofluorescent images of plated cells on the CTRL, F3, and F4 samples are shown in Fig. 6b. In this figure, nuclei were depicted in blue, and phalloidin was depicted in green. The images show that the cells were in a good state and sprawled on the surface of the specimens. Survived cells were well-adherent on the surfaces, even on F4, on which cells did not proliferate according to the viability assay. The good cell adhesion of a few ASCs combined with the high variability (higher statistical error compared to F1 and F3) shown on F4 specimens may find an explanation as follows. A few ion-resistant clones that were capable of surviving during the observation time (3 days), even beyond the DL50 threshold, were selected and F4 was not highly cytotoxic to all mesenchymal cells.

3.4. | *antibiofilm analysis*

As an evaluation of the biofilm inhibition function of coated samples compared to pristine ones, the biofilm quantification by CFU counts was performed. The results are depicted in Fig. 6c. The numbers of CFU/mL $\times 10^5$ of the F1 (pristine Y-TZP sample), F3, and F4 were 3.69 ± 0.98, 1.19 ± 0.88, and 1.22 ± 0.63 respectively. There was a significant difference among the pristine sample (F1), F3, and F4 samples. F3 and F4 samples had significantly lower CFU/mL values than F1. The results indicated the antibiofilm activity of F3 and F4 samples.

Comparing these results with ion release ones (0.34 mg/l for F3 and 0.99 mg/l for F4) and with the MIC reported in the literature (768 μg/ml) [59,60], it seems that the antibacterial mechanism is not only based on the ion release (significantly lower compared to the MIC) but also on a contact-killing mechanism which allows the obtainment of a cytocompatible and antibacterial surface (F3). The similar antibacterial

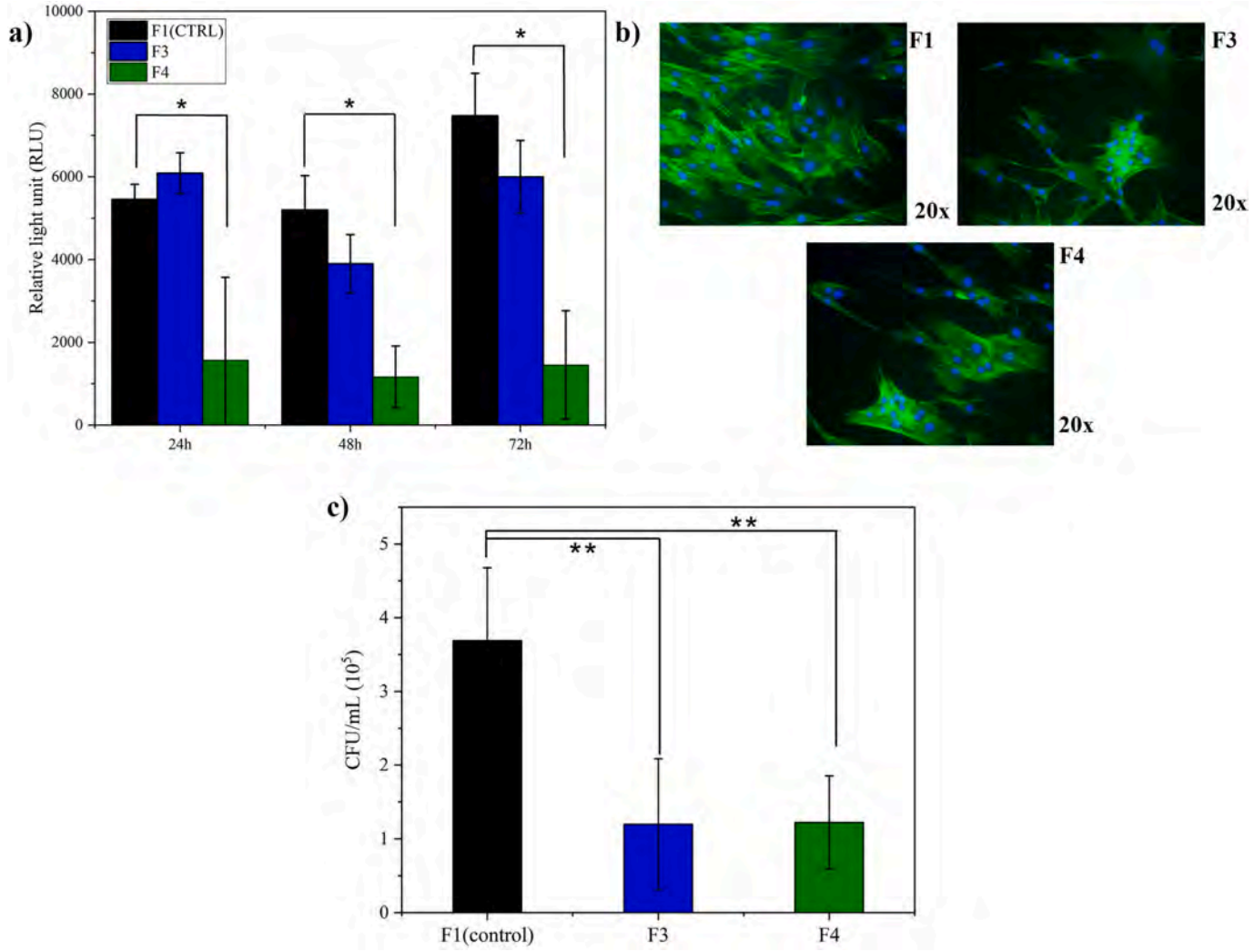

Fig. 6. A) cell viability test after 24, 48, and 72 h of culture. Data represent mean ± std. v; n = 3 independent experiments; * $p < 0.05$; Statistical analysis: ordinary one-way ANOVA (RLU = relative light unit. b) Immunofluorescent images of ASCs cells seeded on the F1(CTRL), F3, and F4 specimens for 24 h. c) Biofilm quantification on pristine and coated samples (Data represent mean ± std. v; n = 3 independent experiments; * $p < 0.05$; Statistical analysis: ordinary one-way ANOVA).

action of F3 and F4 which showed a significant different amount of released zinc ions agrees with this hypothesis. This is not trivial considering that Zn^{2+} ions present a high MIC value and a quite low LD50 value. This means that it is not easy to get antibacterial action and cytocompatibility at the same time on a Zn-doped surface. Some previous studies demonstrated the effectiveness of ZnO nanowires on a silica layer in inactivating over 99 % of bacteria through mechanical rupture mechanisms, while maintaining good compatibility with human cells [65]. Other studies have shown that certain types of materials exhibit contact-killing properties and prolonged antibiofilm activity without the significant release of antimicrobial agents [66].

4. | conclusion

In conclusion, we developed a new cytocompatible SiO_2/ZnO layer with anti-biofilm properties deposited on the Y-TZP substrate for dental applications. For that, a co-sputtering technique was used for the deposition of SiO_2/ZnO layer with different Zn contents (11 and 44 wt %). As a result, the successful deposition of the SiO_2/ZnO layer was confirmed by morphological and chemical characterization techniques including FESEM, EDS, XPS, and FTIR.

The antibiofilm properties of our developed SiO_2/ZnO coating on Y-TZP were investigated on an oral bacterial strain evidencing a combination of ion release and contact-killing mechanism. The results indicated a clear and significant difference between biofilm formation on pristine and coated Y-TZP. Also, the cytocompatibility of SiO_2/ZnO coatings on Y-TZP was investigated using cell viability assays test with adipose-derived mesenchymal stem cells (ASCs). The results showed that one of the developed coated samples had basic requirements for biological compatibility and dental applications due to its cytocompatibility when the zinc content was maintained at low levels. Finally, the hardness of the samples was investigated using the nanoindentation test. The results show an increase in the hardness of the SiO_2-coated sample by introducing ZnO. The results of this study suggest how introducing ZnO to SiO_2 layers can induce antibiofilm properties on dental zirconia, increasing its hardness, and maintaining cytocompatibility.

CRediT authorship contribution statement

Ehsan Shakerinasab: Writing – original draft, Investigation, Conceptualization. **Sara Ferraris:** Writing – original draft, Supervision, Methodology, Investigation. **Sergio Perero:** Writing – original draft, Supervision, Methodology, Investigation, Conceptualization. **Giacomo Maculotti:** Writing – original draft, Investigation. **Maurizio Galetto:**

Supervision. **Anna Luganini:** Writing – original draft, Investigation. **Martina Perin:** Writing – original draft, Investigation. **Federico Mussano:** Writing – original draft, Supervision, Investigation. **Farshad Sohbatzadeh:** Supervision, Conceptualization. **Silvia Spriano:** Writing – original draft, Supervision, Methodology, Conceptualization.

Declaration of competing interest

The authors declare that they have no known competing financial interests or personal relationships that could have appeared to influence the work reported in this paper.

Acknowledgements

This study was carried out within the MICS (Made in Italy – Circular and Sustainable) Extended Partnership and received funding from the European Union Next-GenerationEU (PIANO NAZIONALE DI RIPRESA E RESILIENZA (PNRR) – MISSIONE 4 COMPONENTE 2, INVESTIMENTO 1.3 – D.D. 1551.11-10-2022, PE00000004). This manuscript reflects only the authors' views and opinions, neither the European Union nor the European Commission can be considered responsible for them.

Appendix A. Supplementary data

Supplementary data to this article can be found online at https://doi.org/10.1016/j.apsusc.2025.162590.

Data availability

No data was used for the research described in the article.

References

[1] Stadlinger, B., et al., *Comparison of zirconia and titanium implants after a short healing period. A pilot study in minipigs.* International journal of oral and maxillofacial surgery, 2010. **39**(6): p. 585-592.
[2] F.H. Schünemann, et al., Zirconia surface modifications for implant dentistry, Mater. Sci. Eng. C 98 (2019) 1294–1305.
[3] A. Han, et al., An introduction of biological performance of zirconia with different surface characteristics: a review, Dent. Mater. J. 39 (4) (2020) 523–530.
[4] J.Y. Thompson, B.R. Stoner, J.R. Piascik, Ceramics for restorative dentistry: critical aspects for fracture and fatigue resistance, Mater. Sci. Eng. C 27 (3) (2007) 565–569.
[5] R. Yamada, et al., Ag nanoparticle–coated zirconia for antibacterial prosthesis, Mater. Sci. Eng. C 78 (2017) 1054–1060.
[6] H. Chouirfa, et al., Review of titanium surface modification techniques and coatings for antibacterial applications, Acta Biomater. 83 (2019) 37–54.
[7] C. Hämmerle, Biofilm on dental implants: a review of the literature, Int. J. Oral Maxillofac Implant 24 (2009) 616.
[8] S. Woodhouse, G. Hebbard, S.R. Knowles, Exploring symptom severity, illness perceptions, coping styles, and well-being in gastroparesis patients using the common sense model, Dig. Dis. Sci. 63 (2018) 958–965.
[9] L. Juan, et al., Deposition of silver nanoparticles on titanium surface for antibacterial effect, Int. J. Nanomed. (2010) 261–267.
[10] M.M. Fürst, et al., Bacterial colonization immediately after installation on oral titanium implants, Clin. Oral Implant Res. 18 (4) (2007) 501–508.
[11] Y. Liu, et al., Mussel-inspired organic–inorganic implant coating based on a layer-by-layer method for anti-infection and osteogenesis, Ind. Eng. Chem. Res. 61 (35) (2022) 13040–13051.
[12] Q. Xin, et al., Supramolecular Self-Healing Antifouling Coating for Dental Materials, ACS Appl. Mater. Interfaces 15 (35) (2023) 41403–41416.
[13] Z. Huang, et al., Investigation on the Osteogenic and Antibacterial Properties of Silicon Nitride-Coated Titanium Dental Implants, ACS Biomater Sci. Eng. (2024).
[14] Z. Chen, et al., Overview of antibacterial strategies of dental implant materials for the prevention of peri-implantitis, Bioconjug. Chem. 32 (4) (2021) 627–638.
[15] K.S. Ong, et al., Current anti-biofilm strategies and potential of antioxidants in biofilm control, Expert Rev. Anti Infect. Ther. 16 (11) (2018) 855–864.
[16] J.B. Kaplan, Biofilm matrix-degrading enzymes, Methods and Protocols, Microbial Biofilms, 2014, pp. 203–213.
[17] V.C. Kalia, Quorum sensing inhibitors: an overview, Biotechnol. Adv. 31 (2) (2013) 224–245.
[18] P. Narayana, P. Srihari, Biofilm resistant surfaces and coatings on implants: A review, Mater. Today Proc. 18 (2019) 4847–4853.
[19] M. Liu, et al., Surface modification of zirconia with polydopamine to enhance fibroblast response and decrease bacterial activity in vitro: A potential technique for soft tissue engineering applications, Colloids Surf. B Biointerfaces 136 (2015) 74–83.
[20] J. Sahoo, et al., Nanomaterial-based antimicrobial coating for biomedical implants: new age solution for biofilm-associated infections, ACS Omega 7 (50) (2022) 45962–45980.
[21] M.G. Correa, et al., Antimicrobial metal-based nanoparticles: A review on their synthesis, types and antimicrobial action, Beilstein J. Nanotechnol. 11 (1) (2020) 1450–1469.
[22] K. Gold, et al., Antimicrobial activity of metal and metal-oxide based nanoparticles, Advanced Therapeutics 1 (3) (2018) 1700033.
[23] N. Mohammed, et al., Physical chemical effects of zinc on in vitro enamel demineralization, J. Dent. 42 (9) (2014) 1096–1104.
[24] M.M. Almoudi, et al., A systematic review on antibacterial activity of zinc against Streptococcus mutans, The Saudi Dental Journal 30 (4) (2018) 283–291.
[25] P.P. Mahamuni-Badiger, et al., Biofilm formation to inhibition: Role of zinc oxide-based nanoparticles, Mater. Sci. Eng. C 108 (2020) 110319.
[26] S. Vijayakumar, et al., Laurus nobilis leaf extract mediated green synthesis of ZnO nanoparticles: Characterization and biomedical applications, Biomed. Pharmacother. 84 (2016) 1213–1222.
[27] V. Puspasari, et al., ZnO-based antimicrobial coatings for biomedical applications, Bioprocess Biosyst. Eng. 45 (9) (2022) 1421–1445.
[28] S. Zinelis, et al., Surface characterization of zirconia dental implants, Dent. Mater. 26 (4) (2010) 295–305.
[29] P. Kamonwanon, et al., SiO2-nanocomposite film coating of CAD/CAM composite resin blocks improves surface hardness and reduces susceptibility to bacterial adhesion, Dent. Mater. J. 36 (1) (2017) 88–94.
[30] Y. Yan, et al., Reinforcement of Bonding Strength between Dental Y-TZP and Resin via Nano-Thin and Conformal SiO2 Films by Atomic Layer Deposition, Adv. Mater. Interfaces 10 (5) (2023) 2201910.
[31] P. Kamonwanon, et al., Wear resistance of a modified polymethyl methacrylate artificial tooth compared to five commercially available artificial tooth materials, J. Prosthet. Dent. 114 (2) (2015) 286–292.
[32] R.F. Ribeiro, et al., Y-TZP Physicochemical Properties Conditioned with ZrO2 and SiO2 Nanofilms and Bond Strength to Dual Resin Cement, Materials 15 (22) (2022) 7905.
[33] P. Jevnikar, et al., The effect of nano-structured alumina coating on resin-bond strength to zirconia ceramics, Dent. Mater. 26 (7) (2010) 688–696.
[34] H. Moradpoor, et al., An overview of recent progress in dental applications of zinc oxide nanoparticles, RSC Adv. 11 (34) (2021) 21189–21206.
[35] M. Irfan, et al., Antibacterial, highly hydrophobic and semi transparent Ag/plasma polymer nanocomposite coating on cotton fabric obtained by plasma based co-deposition, Cellul. 26 (2019) 8877–8894.
[36] S. Ferraris, et al., Antibacterial inorganic coatings on metallic surfaces for temporary fixation devices, Appl. Surf. Sci. 508 (2020) 144707.
[37] G.K. Sidhu, et al., Photoluminescence quenching of Zirconia nanoparticle by surface modification, Appl. Surf. Sci. 334 (2015) 216–221.
[38] H.M. Altass, S.K. Abd El Rahman, Surface and catalytic properties of triflic acid supported zirconia: effect of zirconia tetragonal phase, J. Mol. Catal. A Chem. 411 (2016) 138–145.
[39] E. Shakerinasab, et al., A promising method for promoting interfacial adhesion of aramid/rubber composite using atmospheric pressure plasma surface modification, Polym. Compos. (2024).
[40] I. Prasad, A. Chandorkar, Spectroscopy of silicon dioxide films grown under negative corona stress, J. Appl. Phys. 94 (4) (2003) 2308–2310.
[41] H. Qin, et al., Photocatalytic activity of heterostructures based on ZnO and N-doped ZnO, ACS Appl. Mater. Interfaces 3 (8) (2011) 3152–3156.
[42] W. Yu, J. Zhang, T. Peng, New insight into the enhanced photocatalytic activity of N-, C-and S-doped ZnO photocatalysts, Appl Catal B 181 (2016) 220–227.
[43] B. Santra, et al., Tailoring structural, chemical, and photocatalytic properties of ZnO@ β-SiC composites: The effect of annealing temperature and environment, ACS Omega 8 (26) (2023) 24113–24124.
[44] J. Zhang, et al., Hollow chain-like SiO2/ZnO nanocomposites: Electrospinning synthesis, defect-related luminescence, and applications for drug delivery, Colloids Surf A Physicochem Eng Asp 647 (2022) 129139.
[45] D. Wang, et al., Controlled preparation of superparamagnetic Fe3O4@ SiO2@ ZnO-Au core-shell photocatalyst with superior activity: RhB degradation and working mechanism, Powder Technol. 327 (2018) 489–499.
[46] M. Oishi, et al., Surface changes of yttria-stabilized zirconia in water and Hanks solution characterized using XPS, Surf. Interface Anal. 50 (5) (2018) 587–591.
[47] P. Pandoleon, et al., Aging of 3Y-TZP dental zirconia and yttrium depletion, Dent. Mater. 33 (11) (2017) e385–e392.
[48] I. Lisovskyy, et al., Transformation of the structure of silicon oxide during the formation of Si nanoinclusions under thermal annealings, Ukr J Phys 54 (4) (2009) 383–390.
[49] L. Zhang, et al., Thickness measurement of oxide and carbonaceous layers on a 28 Si sphere by XPS, IEEE Trans. Instrum. Meas. 66 (6) (2016) 1297–1303.
[50] H.-P. Ma, et al., Systematic study of the SiOx film with different stoichiometry by plasma-enhanced atomic layer deposition and its application in SiOx/SiO2 super-lattice, Nanomaterials 9 (1) (2019) 55.
[51] J. Zhai, H. Jiang, ZnO@ SiO2 Nanocapsules: Efficient Fluorescence for Latent Fingerprint Detection, ChemistrySelect 8 (25) (2023) e202301101.
[52] A. Kushwaha, M. Aslam, Hydrogen-incorporated ZnO nanowire films: stable and high electrical conductivity, J. Phys. D Appl. Phys. 46 (48) (2013) 485104.
[53] M. Raven, XPS and Auger LMM analysis of ZnO/Si and ZnO/SiO2 interfaces, Surf. Interface Anal. 1 (1) (1979) 20–25.

[54] M.Y. Kim, et al., Detection of nitric oxide from living cells using polymeric zinc organic framework-derived zinc oxide composite with conducting polymer, Small 13 (26) (2017) 1700502.
[55] I. Fatimah, et al., Nanoflower-like composites of ZnO/SiO2 synthesized using bamboo leaves ash as reusable photocatalyst, Arab. J. Chem. 14 (3) (2021) 102973.
[56] S. Spriano, et al., How do wettability, zeta potential and hydroxylation degree affect the biological response of biomaterials? Mater. Sci. Eng. C 74 (2017) 542–555.
[57] D. Lai, G. Kong, C. Che, Synthesis and corrosion behavior of ZnO/SiO2 nanorod-sub microtube superhydrophobic coating on zinc substrate, Surf. Coat. Technol. 315 (2017) 509–518.
[58] F. Gamna, et al., Grafting of alpha-tocopheryl phosphate on chemically treated Ti-6Al-4V for antibacterial bone implants, Appl. Surf. Sci. 619 (2023) 156681.
[59] S. Ferraris, S. Spriano, Antibacterial titanium surfaces for medical implants, Mater. Sci. Eng. C 61 (2016) 965–978.
[60] W.-L. Du, et al., Antibacterial activity of chitosan tripolyphosphate nanoparticles loaded with various metal ions, Carbohydr. Polym. 75 (3) (2009) 385–389.
[61] F. Heidenau, et al., A novel antibacterial titania coating: metal ion toxicity and in vitro surface colonization, J. Materials Science: Materials in Medicine 16 (2005) 883–888.
[62] B. Tian, Y. Liu, Antibacterial applications and safety issues of silica-based materials: a review, Int. J. Appl. Ceram. Technol. 18 (2) (2021) 289–301.
[63] M. Cierech, et al., Zinc oxide nanoparticles cytotoxicity and release from newly formed PMMA–ZnO nanocomposites designed for denture bases, Nanomaterials 9 (9) (2019) 1318.
[64] E. Paszek, et al., Zinc oxide nanoparticles impair the integrity of human umbilical vein endothelial cell monolayer in vitro, J. Biomed. Nanotechnol. 8 (6) (2012) 957–967.
[65] T. Shimada, et al., Mechanical rupture-based antibacterial and cell-compatible ZnO/SiO2 nanowire structures formed by bottom-up approaches, Micromachines 11 (6) (2020) 610.
[66] H. Mitwalli, et al., Emerging contact-killing antibacterial strategies for developing anti-biofilm dental polymeric restorative materials, Bioengineering 7 (3) (2020) 83.